Received: 1 August 2019 | Revised: 1 October 2019 | Accepted: 11 October 2019

DOI: 10.1002/inf2.12070

ORIGINAL ARTICLE

WILEY

Vapor phase fabrication of three-dimensional arrayed BiI_3 nanosheets for cost-effective solar cells

Yiyi Zhu[1,2] | Qianpeng Zhang[1,2] | Matthew Kam[1,2] | Swapnadeep Poddar[1,2] | Leilei Gu[1,2] | Shijun Liang[3] | Pengfei Qi[4] | Feng Miao[3] | Zhiyong Fan[1,2]

[1]HKUST-Shenzhen Research Institute, Shenzhen, China

[2]Department of Electronics and Computer Engineering, Hong Kong University of Science and Technology (HKUST), Hong Kong, SAR, China

[3]National Laboratory of Solid State Microstructures, School of Physics, School of Electronic Science and Engineering, Collaborative Innovation Centre of Advanced Microstructures, Nanjing University, Nanjing, China

[4]Zhong Shan Rui Ke New Energy Co. Ltd., Zhongshan, Guangdong, China

Correspondence
Zhiyong Fan, HKUST-Shenzhen Research Institute, No. 9 Yuexing First RD, South Area, Hi-Tech Park, Nanshan, Shenzhen 518057, China.
Email: eezfan@ust.hk

Funding information
General Research Fund, Grant/Award Number: 16237816; National Key Basic Research Program of China, Grant/Award Number: 2015CB921600; National Natural Science Foundation of China, Grant/Award Numbers: 51672231, 61574076; Natural Science Foundation of Jiangsu Province, Grant/Award Number: BK20180330; the Science and Technology Plan of Shenzhen, Grant/Award Number: JCYJ20170818114107730

Abstract

Multilayered photovoltaic absorbers have triggered widespread attention for their unique structure and properties. However, multilayered materials in the randomly oriented polycrystalline thin-film lead to ineffective carrier transport and collection, which hinders the process of achieving high-performance solar cells. Herein, this issue is tackled by producing the three-dimensional (3D) heterojunction BiI_3 nanosheets (NSs) solar cells, which embed vertically aligned monocrystalline BiI_3 NSs into spiro-OMeTAD. The preferred orientation of BiI_3 NSs and large p-n junction areas of 3D heterojunction structure enable a strong light absorption and effective carrier transport and collection, and thus a power conversion efficiency (PCE) of 1.45% was achieved. Moreover, this PCE is the highest ever reported for BiI_3 based solar cells to our best knowledge. Moreover, the nonencapsulated device remained 96% of the initial PCE after 24 h continuous one sun illumination at ~70% humidity condition, and 82% of the initial PCE after 1-month storage at ~30% humidity condition.

KEYWORDS

3D solar cells, BiI_3, multilayered semiconductors

1 | INTRODUCTION

Solar energy is one of the most abundant sustainable energy resources in the world. Despite years of research, searching for a cost-effective, efficient, nontoxic, and air-stable alternative photovoltaic absorber is still the key to achieve the new-generation high-performance solar cells. One of the promising candidates is BiI_3, which is a layered heavy metal-semiconductor previously investigated for X-ray imaging and gamma-ray detection.[1-3] Until recently, BiI_3 caught

researchers' attention for photovoltaic application due to the proper bandgap (1.43-2.2 eV),[4] high absorption coefficient (10^5 cm^{-1}),[5] high electron mobility (200 ± 50 cm^2 V^1 s^{-1}),[6] and low carrier concentration (10^8 cm^{-3}).[7] BiI_3 molecule is constructed by repeating the unit of the I-Bi-I plane. Strong ionic I–Bi bond and weak van der Waals I-I interaction exist within each plane and in between planes, respectively.[8] Primarily because of its layer-by-layer structure, BiI_3 exhibits interesting anisotropic electronic and optical properties.[9] The valence band maximum (VBM) is dominated by I-p states, and the conduction band minimum (CBM) is mainly contributed by I-p and Bi-p states.[4,10] For the VBM and CBM that are parallel to the I-Bi-I plane,[4,10] carriers are mobile within planes but immobile across planes. Meanwhile, BiI_3 exhibits highly asymmetric carrier mobilities. Brandt et al[11] reported the effective hole and electron masses of BiI_3 to be 10.39 and 1.85, respectively. The electron mobility is 27.7 times higher than hole mobility.[1,12] Due to the above properties, the carrier transport and collection in the randomly oriented polycrystalline BiI_3 thin-film are not effective,[13] which leads to the inferior photovoltaic performance. Until now, the best-reported PCEs for BiI_3 solar cells are still lower than 1.1%. For instance, Lehner et al[14] applied BiI_3 for a heterojunction planar solar cell and achieved a PCE around 0.3%. Hamdeh et al[15] explored solution-processed BiI_3 based solar cells with 0.09% PCE and observed the improved performance of 1.02% PCE with solvent vapor annealing.

To tackle the issues discussed above, the BiI_3 should be synthesized as vertically aligned nanosheets (NSs) along the preferential alignment direction of I-Bi-I planes.[13] Moreover, the naturally passivated surface of BiI_3 NSs alleviates surface recombination.[16] However, controllable mass production of BiI_3 NSs for solar cells was limited by the intricate transfer process of NSs.[17-19]

Here, we demonstrated a 3D heterojunction structure. The vertically aligned monocrystalline BiI_3 NSs grown on SnO_2/FTO glass were embedded into 2,2′,7,7′-tetrakis-(*N*, *N*-di-4-methoxyphenylamino)-9,9′-spirobifluorene) (spiro-OMeTAD). Notably, our work shows the ability to synthesize the monocrystalline BiI_3 NSs with controlled grain size. Importantly, we developed a cost-effective, scalable, and transfer-free process in this work, and achieved a PCE of 1.45% which is the highest reported to our best knowledge. Moreover, the strategy developed in this work can also be applied to other multilayered materials such as graphene,[20-22] 2D perovskites,[23-28] and transition metal dichalcogenides.[29-32]

2 | RESULTS AND DISCUSSIONS

Figure 1A shows a diagram of the device fabrication process. A detailed process can be found in Section 4. BiI_3 NSs were directly grown by the vapor-solid-solid (VSS) reaction between Bi and I_2, which ensures a high material quality.[33,34] Figure 1A shows a cross-sectional schematic diagram of BiI_3 NSs cell. Figure 1C shows the band-energy diagram of the complete device. Band energy levels of SnO_2,[35] BiI_3,[14] and spiro-OMeTAD[36] were all found in the literature. Because of the electrons dominated carrier transport behavior of BiI_3, the orthogonalization of electron and hole collection in 3D heterojunction structure enables a more efficient separation and collection.[37,38] Besides, as carriers are mobile within I-Bi-I planes but immobile across planes in BiI_3, the vertically aligned orientation facilities carrier transport in the device.[13] Moreover, the narrow width of BiI_3 NSs enables more effective separation of electron-hole pairs into free carriers, especially for the short carrier lifetime photovoltaic absorbers like BiI_3.[37]

The scanning electron microscopy (SEM) image in Figure 2A shows the morphology of BiI_3 NSs from the precursor (30 nm Bi) grown on the substrate. The BiI_3 NSs were uniformly distributed and vertically aligned with lateral size ranging from 200 to 400 nm and thickness around 50 nm. Figure 2B shows a tilted angle (60°) SEM image of BiI_3 NSs with a height of around 260 nm. Figure 2C and Figure S1 show the SEM images of BiI_3 embedded in the spiro-OMeTAD. Figure 2D is the transmission electron microscopy (TEM) image, which reveals a hexagonal NS structure with clear lattice fringes, confirming a monocrystalline nature of BiI_3 NSs. Figure 2E is the enlarged view that shows the lattices spacing of 3.7 Å between (110) planes. The selected area electron diffraction pattern in Figure 2F exhibits diffraction spots in a hexagonal symmetry, which also indicates the high crystallinity.[18,39]

The epitaxial growth of NSs involves many complex processes, for instance, the decomposition of the precursor, the diffusion of reactant, the atomic structure of the surface and the adsorption and desorption of atoms at growth front, and so forth.[40] Compared with the typical horizontally oriented NSs, we attributed the synthesis of vertically aligned BiI_3 NSs to the edge-growth mechanism and growth competition among different orientated BiI_3 NSs. The Bi precursor is a layer of uniformly distributed nanoparticles (Figure S2a). Equation 1 shows the chemical reaction between indium vapor and solid-state Bi nanocrystal[41] at 100°C. The growth is by the VSS mechanism. The schematic of the BiI_3 NSs formation process is explicated in Figure S3. Because I-Bi-I layers are dangling-bond-free surfaces and cannot serve as effective nucleation sites for lateral epitaxy, the BiI_3 formation process follows an edge-growth mechanism and NSs were synthesized. Furthermore, for the indium diffusivity in the solid-state Bi-metal is not efficient at 100°C, the

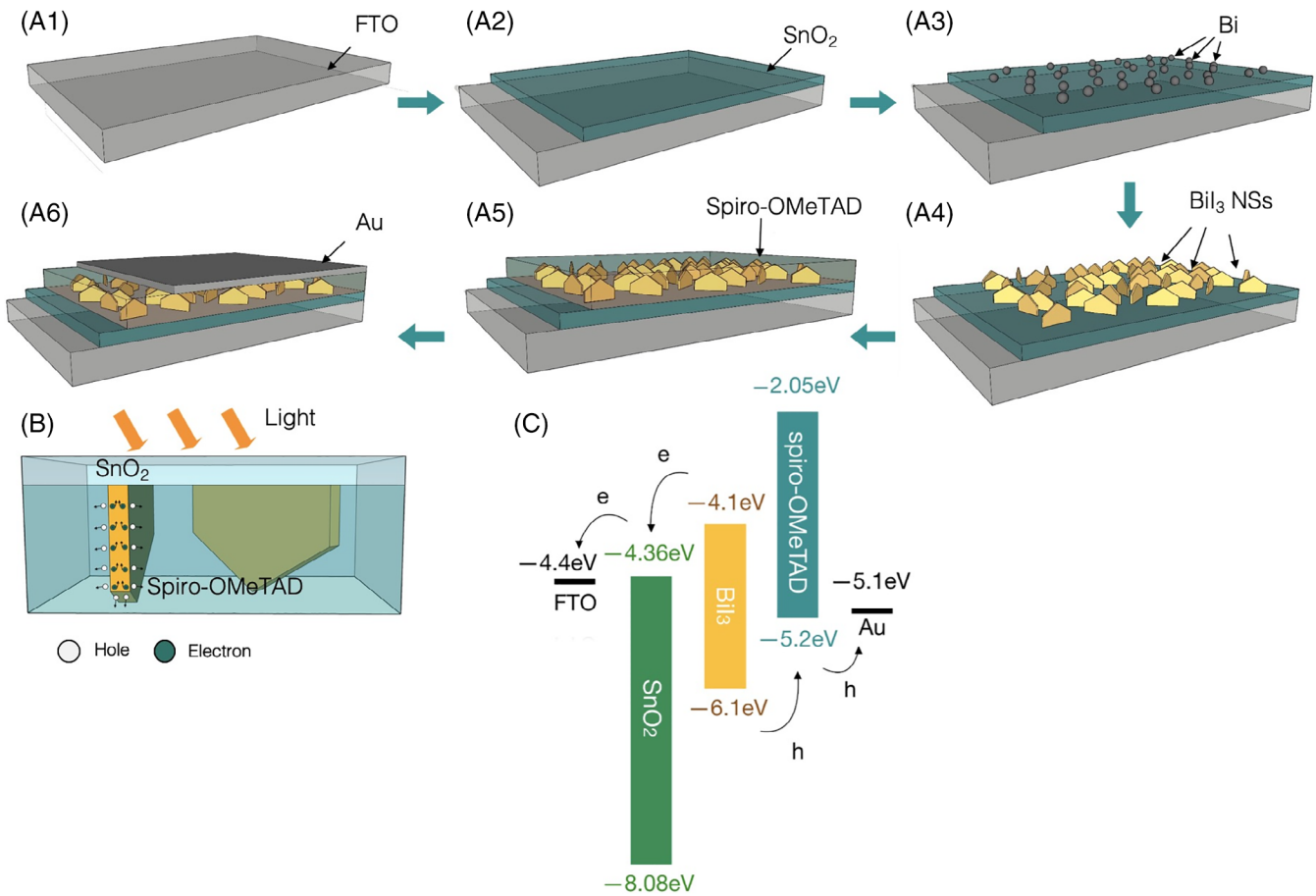

FIGURE 1 Diagram of the device fabrication process: (A1) cleaning of FTO glass, (A2) sputtering of SnO_2, (A3) evaporation of Bi, (A4) VSS growth of BiI_3 NSs, (A5) deposition of Spiro-OMeTAD and (A6) deposition of top contact. (B) Cross-sectional schematic diagram of BiI_3 NSs cell. (C) Band-energy diagram of the complete device

diffusion process is the control step.[42,43] Depicted in Figure S3, the horizontal-aligned BiI_3 NSs at the surface of the Bi precursor hinders the diffusion process, with a result, the supply of indium is not as sufficient as the vertically aligned NSs. Consequently, the horizontal-aligned BiI_3 NSs has the slowest growth rate, and vertically aligned orientation is the dominated orientation.

$$2\mathrm{Bi}\,(\mathrm{s}) + 3\mathrm{I}_2(\mathrm{g}) \rightarrow 2\mathrm{BiI}_3(\mathrm{s}). \quad (1)$$

The NSs grain size is always associated with the synthesis condition, for instance, the precursor thickness, temperature, reaction time, and so forth.[43] In this work, vertically aligned BiI_3 NSs were synthesized under different conditions. The results show that the temperature variation (90°C-110°C) and reaction time (1-3 h) do not have a great impact on the BiI_3 NSs grain size, the related discussion can be found in Figures S4 and S5. However, shown in Figure S2, the BiI_3 grain size increased with the raise of precursor thickness. This implies that the final grain size is determined by the amount of the precursor in the I-rich growth condition, which can be indicated by the Bi thickness.[44] More importantly, the preferred orientation is independent of precursor thickness, which was also verified by both the SEM (Figure S2) and X-ray diffraction (XRD) (Figure 3A) results. Therefore, the crystal size can be precisely controlled by the Bi thickness. The controlled morphology of vertically aligned BiI_3 NSs enables a future study of NSs geometry effect on device performance.[33,34]

To study the crystal structure of BiI_3 NSs, the XRD patterns of as-grown BiI_3 NSs with different Bi precursor thicknesses on the SnO_2/FTO substrate were characterized. As shown in Figure 3A, the XRD patterns match well with the mixed peaks of tetragonal structure of SnO_2 (Space-group: P42/mnm(136) with lattice constants of a = 4.75 Å, c = 3.20 Å) and hexagonal structure of BiI_3 (PDF no. 48–1795, Space-group:R–3(148) with lattice constants of a = 7.52 Å and c = 20.72 Å).[45,46] The XRD patterns from different precursor thicknesses all show a higher relative intensity of diffraction peak from the (300) plane at 41.57° compared to that of the BiI_3 powder reference. The I-Bi-I plane stacked along the [003] direction, the results confirm that BiI_3 NSs were in the

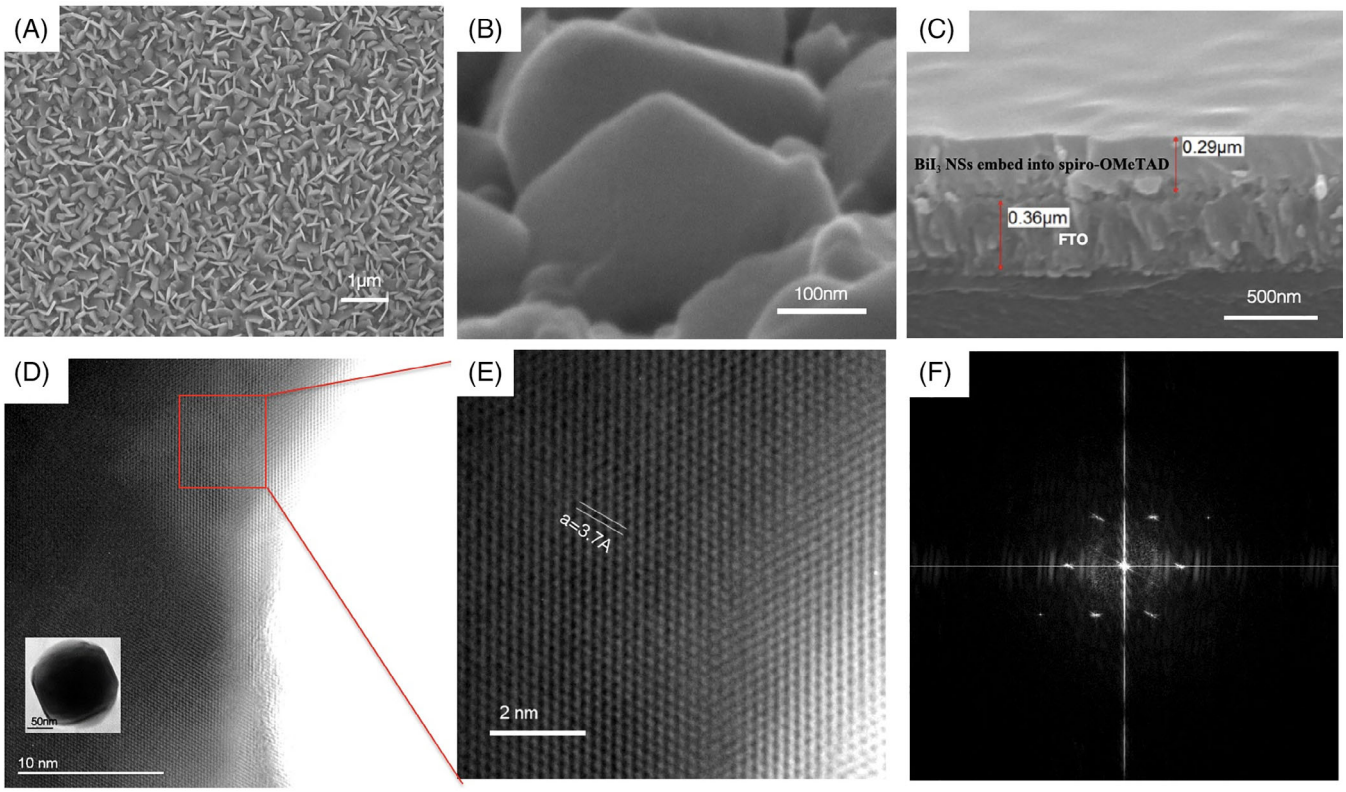

FIGURE 2 (A) Top-view SEM images of BiI_3, (B) Tilted-angle view (60°) SEM image of BiI_3 NSs, (C) Cross-sectional SEM images of (from bottom to top) FTO/SnO_2/BiI_3 NSs/Spiro-OMeTAD, (D) TEM image of BiI_3 NSs, (E) Zoomed-in image of the red dash rectangular area in (D), (F) SAED pattern of BiI_3 NSs (FFT filtered images)

preferential alignment of I-Bi-I plane, which is perpendicular to the substrate.[47] Besides, the low diffraction background and sharp diffraction peaks indicate the high crystallinity of BiI_3 NSs, and no redundant diffraction peak is observed.

The bandgap of BiI_3 has been determined both experimentally and computationally with values ranging from 1.43 to 2.2 eV.[4] UV–visible spectrophotometry was performed for BiI_3 NSs on the glass. As extrapolated in the Tauc plot in Figure 3B, the BiI_3 NSs is an indirect bandgap material (E_g ~ 1.74 ± 0.05 eV), which agrees with the experimental results[48,49] and first principle analysis.[49] Depicted in Figure 3B and Figure S6, there is an enhanced light absorption from the antireflection effect. The average refection of BiI_3 NSs based on 20, 30, 40 nm Bi precursor over 400-900 nm range are 14.5%, 3.0%, and 2.4%, respectively. The corresponding reflection spectra are plotted in Figure S6. Moreover, the average refection of BiI_3 (Bi 30 nm) is one order of magnitude lower than that of the planar BiI_3.[15] The anti-reflection property is attributed to the light trapping nature of the NSs. Related discussion can be found with optical simulation results shown in Figure S7. Moreover, the anti-reflection effect enhanced with the increase of precursor Bi thickness, which is caused by the improved filling ratio and the increased height of BiI_3 NSs (Figure S2). The absorption of BiI_3 (Bi 30 nm) reached as high as 95% at wavelength below 650 nm and has a clear cutoff at 670 nm and no sub-bandgap or impurity absorption signal is observed.

Figure 3C,D shows the photoluminescence (PL) and time-resolved photoluminescence (TRPL) of BiI_3 NSs, respectively. The PL spectra were obtained with 514 nm excitation, and a PL peak at 670 nm was observed. The TRPL of BiI_3 NSs (red dots) was obtained with 365 nm excitation, and the instrumental response function is shown with black dots. With the mono-exponential fitting, the effective lifetime was estimated to be within the range from τ ~ 0.54 to 0.56 ns (Figure 3D and Figure S8). The effective carrier lifetime is consistent with the previous report.[11,15,49]

Moreover, solar cell devices with FTO/SnO_2/BiI_3 NSs/spiro-OMeTAD/Au structure were fabricated. Figure 4A shows the current density-voltage (*J*-*V*) curves and the external quantum efficiency (EQE) of champion devices, and the device performances are summarized in Table S1. The champion device based on 30 nm Bi film demonstrated the highest PCE of 1.45% with a short-circuit current density (J_{sc}) of 6.36 mA cm^{-2}, an open-circuit voltage (V_{oc}) of 0.47 V, and a fill factor (FF) of 48.52%. Additionally, the device shows EQE values

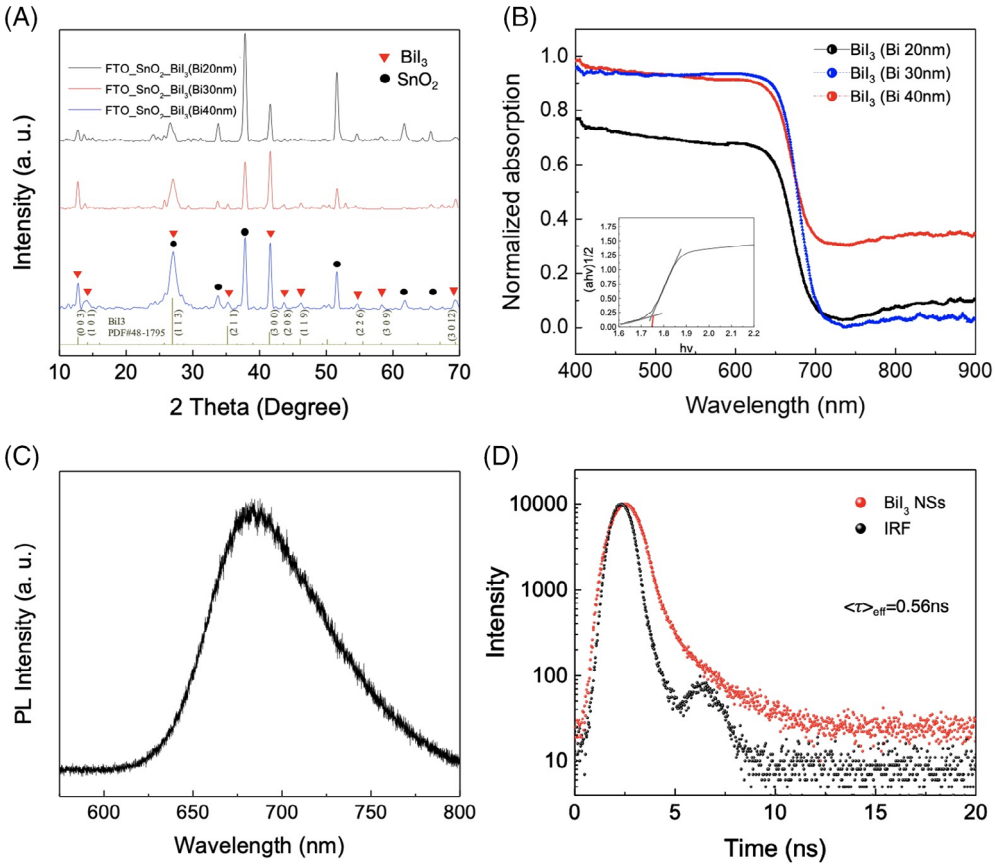

FIGURE 3 (A) X-ray diffraction patterns of (from bottom to top) FTO/SnO_2/BiI_3 (BiI_3 based on different precursor Bi thickness), (B) UV–vis absorption spectra and T_{auc} plot of glass/BiI_3 (BiI_3 based on different precursor Bi thickness), (C) the Steady-state photoluminescence (PL) spectra, (D) Time-resolved photoluminescence spectrum of BiI_3

between 30% and 39% at a wavelength range from 400 to 650 nm. The calculated J_{sc} from EQE spectra was 6.02 mA cm^{-2}. Moreover, from the EQE spectra, there is a poor photo-generated carrier extraction of higher-energy photons. This implies the recombination of electron-hole pairs for higher-energy photons that preferentially absorbed at the SnO_2/BiI_3 interface.[15] The EQE result suggests a need for interface engineering to enhance the performance of the BiI_3 solar cell. A possible strategy is to insert a buffer layer (such as CdS,[50] $CuInS_2$,[51] or ZnS[52]) between SnO_2 and BiI_3 to overcome the low electron collection. In Figure 4A, the low dark saturated current at low bias indicates less trap-assisted recombination in 3D devices compared with the polycrystalline thin film counterpart.[16,53,54] The less trap-assisted recombination is due to the reason that the self-passivated surface of vertically aligned BiI_3 suppressed the carrier recombination at the BiI_3/spiro-OMeTAD interface. Notably, our devices show the highest reported PCE based on BiI_3 to our best knowledge, and the comparison of our work and other reported work is shown in Table S2. The enhanced performance is attributed to less trap-assisted recombination in the superior crystallinity BiI_3, and a more efficient photogenerated carrier separation and collection in the 3D device.[13,24] In addition, the light-trapping structure of 3D arrayed BiI_3 NSs minimizes the number of unabsorbed photons and therefore enhances the photocurrent.[55]

Figure 4B shows the precursor thickness effect on the device performance and the photographs of the corresponding device are shown in Figure S9. The BiI_3 NSs solar cell based on 20 nm Bi exhibited a PCE of 0.62% (J_{sc} = 2.92 mA cm^{-2}, V_{oc} = 0.44 V, and FF = 48.42%). Its lower PCE than the champion device was attributed to the less light absorption. However, as shown in Figure 4B and Table S3, a decrease of PCE was observed when Bi thickness surpassed 30 nm.

Besides the PCE, device stability is another essential concern for practical application. As the grain boundary provides charge accumulation sites and infiltration pathways for moisture and oxygen, they become the most vulnerable sites for device degradation.[39] Thanks to the self-passivated surface and monocrystalline nature of BiI_3 NSs, the NSs device showed decent stability. Figure 4C is

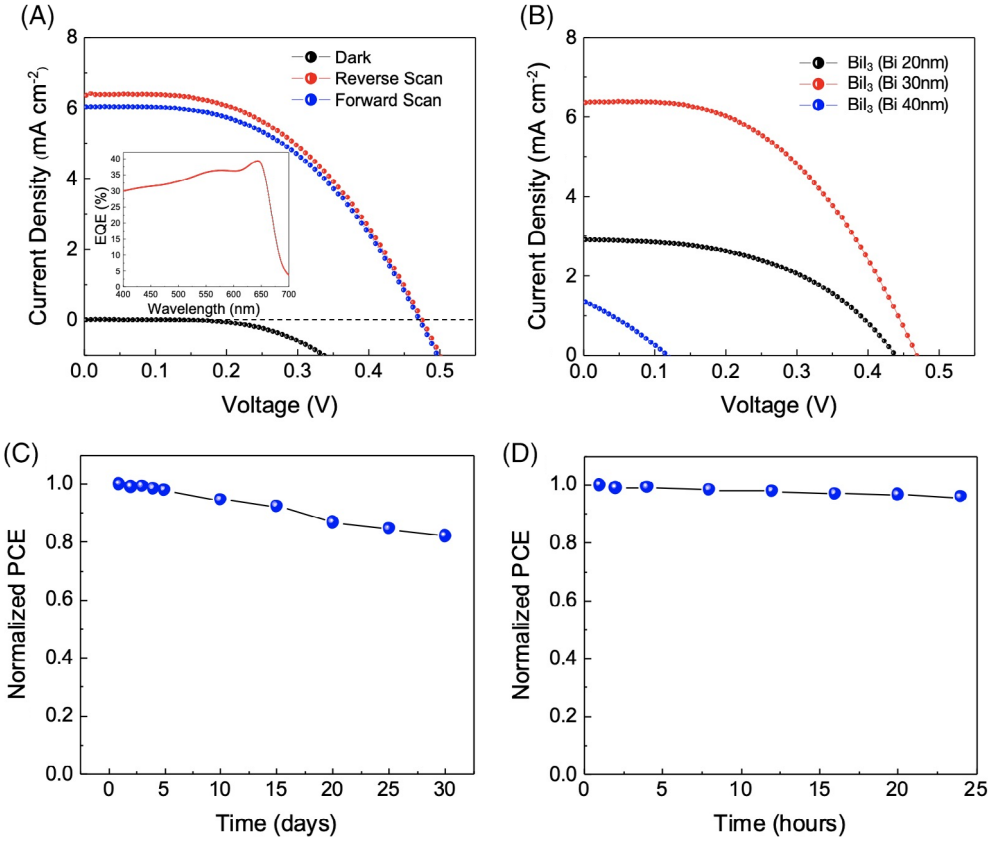

FIGURE 4 (A) *J-V* characteristic and external quantum efficiency (EQE) of the best-performing BiI_3 solar cells with device area of 0.0314 cm^2, (B) *J-V* characteristic of BiI_3 solar cells based on different Bi thickness, (C) The PCE stability of a high-performance BiI_3 solar cell without encapsulation stored in a desiccator with humidity of 30 ± 5%, and (D) stability tests of BiI_3 solar cells exposed in continuous AM1.5G illumination (100 mW cm^{-2}) for 24 h in the ambient condition with a humidity of 70 ± 5%

a long-term stability test of the champion device stored in a desiccator with humidity 30 ± 5% without encapsulation. Moreover, the devices were tested in an ambient environment at 25°C and with 60-90% humidity, maintained 82% of its initial PCE after 30 days. Most importantly, the BiI_3 NSs device also exhibits extraordinary stability under continuous light saturation conditions. Figure 4D shows that the tested devices without packaging remained 96% of its initial PCE after 24 h of continuous AM1.5G illumination (100 mW cm^{-2}) in the ambient condition with a high humidity of 70 ± 5%. These results demonstrate that BiI_3 NSs are air-stable and can be a competitive choice for the photovoltaic light absorber.

3 | CONCLUSIONS

In summary, we reported the 3D heterojunction BiI_3 NSs solar cells with the highest PCE of 1.45% to our best knowledge, and we attributed the high performance to the superior crystallinity of BiI_3 and the efficient photogenerated carrier separation and collection in the 3D device. Our study demonstrates the capability of synthesizing high crystallinity monocrystalline BiI_3 NSs with a controlled grain size. More significantly, our BiI_3 solar cell showed decent stability. The nonencapsulated device remained 96% of its initial PCE after 24 h of continuous (AM1.5G) illumination and 82% after month storage in 30 ± 5% humidity. With the knowledge gained in this work, BiI_3 proves its strong potential for less toxic, efficient and long-term stable solar cells. Moreover, the vapor growth strategy developed here can also be widely used for other multilayered materials.

4 | EXPERIMENTAL SECTION

4.1 | Substrate preparation

The BiI_3 NSs solar cells were fabricated on FTO glass, which was ultrasonically cleaned by detergent, acetone, isopropanol, and deionized water in sequence. After blowing dry the substrate with N_2, 40 nm thick SnO_2 was sputtered as the electron transport layer with a deposition rate of 0.6 Å s^{-1}. The DC sputtering uses an Sn target and

a gas flow rate of 5 sccm O_2 and 50 sccm Ar at 60 W power. After that, Bi-metal with different thicknesses was thermally evaporated with a deposition rate of 1 Å s^{-1}.

4.2 | Vapor phase growth of BiI_3 NSs

The growth of BiI_3 NSs was a vapor-solid-solid reaction carried out in a furnace (OTF 1200X-II, MTI) with a quartz tube. The as-prepared substrates and iodine powder were placed into two small quartz containers at the center of the quartz tube. The iodine powder was spread uniformly inside one quartz container, and the substrate was placed close to the opening end of another container. Thereafter, the growth was performed at 100°C for 1 h with the Ar flow rate of 300 sccm. Iodine vapor is transported toward the sample by Ar gas. After growth, the samples were transferred into a nitrogen-filled glove box.

4.3 | Hole transport layer and top-contact depositions

To embed the BiI_3 NSs into the hole transport layer, a solution of spiro-OMeTAD (80 mg mL^{-1} chlorobenzene) was spin-coated at 1500 rpm for 30 s. After that, 100 nm-thick gold was thermally evaporated at a rate of 1 Å s^{-1} as the top electrode.

4.4 | Characterization

The as-grown BiI_3 NSs were characterized by the XRD (Bruker D8 X-ray Diffractometer, USA) utilizing Cu Kα radiation, TEM (JEOL [2010F] under an accelerating voltage of 200 V), and scanning electron microscopy (FESEM, JEOL JSM-7100F, TESCAN VEGA3). Ultraviolet-visible spectroscopy (Varian Cary 500) was used to obtain the absorption and reflection spectra. PL and TRPL were measured with an FS5 fluorescence spectrometer. Carrier lifetime was convolved with mono-exponential decay fittings. The device performance was measured with an AM© solar simulator (Abet Class AAB Sun 2000, calibrated by a KG5-filtered Si reference cell). The current density-voltage (*J-V*) curves were measured with a Keithley 2400. To calculate the EQE, the photocurrent under monochromatic illuminations at different wavelengths was measured by using a 150 W xenon lamp and a monochromator.

ACKNOWLEDGMENTS

This work was supported by the Science and Technology Plan of Shenzhen (JCYJ20170818114107730), National Natural Science Foundation of China (Project No. 51672231), The General Research Fund (Project No. 16237816) from the Hong Kong Research Grant Council, Natural Science Foundation of Jiangsu Province (Project No. BK20180330), National Natural Science Foundation of China (Project No. 61574076), and National Key Basic Research Program of China (Project No. 2015CB921600).

CONFLICT OF INTEREST

The authors declare no conflict of interest.

ORCID

Zhiyong Fan https://orcid.org/0000-0002-5397-0129

REFERENCES

1. Lintereur AT, Qiu W, Nino JC, Baciak JJNI. Characterization of bismuth tri-iodide single crystals for wide band-gap semiconductor radiation detectors. *Nucl Instrum Methods Phys Res Sect A*. 2011;652(1):166-169.
2. Matsumoto M, Hitomi K, Shoji T, Y H. Bismuth tri-iodide crystal for nuclear radiation detectors. *IEEE Trans Nucl Sci*. 2002;49(5):2517-2520.
3. Owens A. Semiconductor materials and radiation detection. *J Synchrotron Radiat*. 2006;13(2):143-150.
4. Podraza NJ, Qiu W, Hinojosa BB, et al. Band gap and structure of single crystal BiI_3: resolving discrepancies in literature. *J Appl Phys*. 2013;114(3):033110.
5. Jellison G, Ramey J, Boatner LA. Optical functions of BiI_3 as measured by generalized ellipsometry. *Phys Rev B*. 1999;59(15):9718.
6. Zhang W-B, Xiang L-J, H-B L. Theoretical perspective of energy harvesting properties of atomically thin BiI_3. *J Mater Chem A*. 2016;4(48):19086-19094.
7. Ikeda M, Oka Y, Mori K, Atsuta M. Study of dark current blocking layer for BiI/sub 3/X-ray detector film. Paper presented at: Nuclear Science Symposium Conference Record, IEEE 2004, 2004.
8. Wyckoff RWG. *Crystal Structures*. Vol 1. New York: Interscience; 1963:796-797.
9. Geim AK, Grigorieva IVJN. Van der Waals heterostructures. *Nature*. 2013;499(7459):419.
10. Yan H, Ziyu H, Xu G, Xiaohong SJCPL. Structural, electronic and photocatalytic properties of atomic defective BiI_3 monolayers. *Chem Phys Lett*. 2018;691:341-346.
11. Brandt R, Kurchin RC, Hoye R, et al. Investigation of bismuth triiodide (Bil(3)) for photovoltaic applications. *J Phys Chem Lett*. 2015;6(21):4297-4302.
12. Ma F, Zhou M, Jiao Y, et al. Single layer bismuth iodide: computational exploration of structural, electrical, mechanical and optical properties. *Sci Rep*. 2015;5:17558.
13. Xiao Z, Meng W, Wang J, Mitzi DB, Yan YJMH. Searching for promising new perovskite-based photovoltaic absorbers: the importance of electronic dimensionality. *Mater Horizon*. 2017;4(2):206-216.
14. Lehner AJ, Wang H, Fabini DH, et al. Electronic structure and photovoltaic application of BiI_3. *Appl Phys Lett*. 2015;107(13):131109.

15. Hamdeh UH, Nelson RD, Ryan BJ, Bhattacharjee U, Petrich JW, MGJCoM P. Solution-processed BiI_3 thin films for photovoltaic applications: Improved carrier collection via solvent annealing. *Chem Mater*. 2016;28(18):6567-6574.
16. Wang L, Huang L, Tan WC, et al. 2D photovoltaic devices: progress and prospects. 2018;2(3):1700294.
17. Wei Q, Chen J, Ding P, et al. Synthesis of easily-transferred 2D layered BiI_3 nanoplates for flexible visible-light photo-detectors. *ACS Appl Mater Interfaces*. 2018;10(25):21527-21533.
18. Li J, Guan X, Wang C, et al. Synthesis of 2D layered BiI_3 nanoplates, BiI_3/WSe_2 van der Waals heterostructures and their electronic, optoelectronic properties. *Small*. 2017;13(38):1701034.
19. Li J, Guan X, Wang C, et al. Nanoplates: synthesis of 2D layered BiI_3 nanoplates, BiI_3/WSe_2 van der Waals heterostructures and their electronic, optoelectronic properties (small 38/2017). *Small*. 2017;13(38):1701034.
20. Bernardi M, Palummo M, Grossman JC. Extraordinary sunlight absorption and one nanometer thick photovoltaics using two-dimensional monolayer materials. *Nano Lett*. 2013;13(8):3664-3670.
21. Liu Z, Liu Q, Huang Y, et al. Organic photovoltaic devices based on a novel acceptor material: graphene. *Adv Mater*. 2008;20(20):3924-3930.
22. Alamri AM, Leung S, Vaseem M, Shamim A, He J-H. Fully inkjet-printed photodetector using a graphene/perovskite/graphene heterostructure. *IEEE Trans Electron Devices*. 2019;66(6):2657-2661.
23. Cao DH, Stoumpos CC, Farha OK, Hupp JT, Kanatzidis MG. 2D homologous perovskites as light-absorbing materials for solar cell applications. *J Am Chem Soc*. 2015;137(24):7843-7850.
24. Tsai H, Nie W, Blancon J-C, et al. High-efficiency two-dimensional Ruddlesden–Popper perovskite solar cells. *Nature*. 2016;536(7616):312.
25. Smith IC, Hoke ET, Solis-Ibarra D, McGehee MD, Karunadasa HIJAC. A layered hybrid perovskite solar-cell absorber with enhanced moisture stability. *Angew Chem*. 2014;126(42):11414-11417.
26. Kagan C, Mitzi D, Dimitrakopoulos CJS. Organic-inorganic hybrid materials as semiconducting channels in thin-film field-effect transistors. *Science*. 1999;286(5441):945-947.
27. Wang L, Zou X, Lin J, et al. Perovskite/black phosphorus/MoS_2 photogate reversed photodiodes with ultrahigh light on/off ratio and fast response. *ACS Nano*. 2019;13(4):4804-4813.
28. Dong R, Lan C, Xu X, et al. Novel series of quasi-2D Ruddlesden–Popper perovskites based on short-chained spacer cation for enhanced photodetection. *ACS Appl Mater Interfaces*. 2018;10(22):19019-19026.
29. Pezeshki A, Shokouh SHH, Nazari T, Oh K, Im SJAM. Electric and photovoltaic behavior of a few-layer α-$MoTe_2/MoS_2$ dichalcogenide heterojunction. *Adv Mater*. 2016;28(16):3216-3222.
30. Tsai M-L, Su S-H, Chang J-K, et al. Monolayer MoS_2 heterojunction solar. *Cells*. 2014;8(8):8317-8322.
31. Tributsch HJBBC. The $MoSe_2$ electrochemical solar cell: anodic coupling of electron transfer to d → d photo-transitions in layer crystals. *Ber Bunsengesellschaft Phys Chem*. 1978;82(2):169-174.
32. Zhang L, Yang X, Jiang Q, et al. Ultra-bright and highly efficient inorganic based perovskite light-emitting diodes. *Nat Commun*. 2017;8:15640.
33. Schmidt P, Binnewies M, Glaum R, Schmidt M. Chemical vapor transport reactions–methods, materials, modeling. *Advanced Topics on Crystal Growth*. London: IntechOpen; 2013.
34. Binnewies M, Glaum R, Schmidt M, Schmidt P. *Chemical Vapor Transport Reactions*. Berlin, German: Walter de Gruyter; 2012.
35. Kam M, Zhu Y, Zhang D, Gu L, Chen J, Fan Z. Efficient mixed-cation mixed-halide perovskite solar cells by all-vacuum sequential deposition using metal oxide electron transport layer. *Solar RRL*. 2019;3(7):1900050.
36. Bi D, Tress W, Dar MI, et al. Efficient luminescent solar cells based on tailored mixed-cation perovskites. *Sci Adv*. 2016;2(1):e1501170.
37. Fan Z, Razavi H, Do J-w, et al. Three-dimensional nanopillar-array photovoltaics on low-cost and flexible substrates. *Nat Mater*. 2009;8(8):648.
38. Yu M, Long Y-Z, Sun B, Fan ZJN. Recent advances in solar cells based on one-dimensional nanostructure arrays. *Nanoscale*. 2012;4(9):2783-2796.
39. Prasad MD, Sangani LV, Batabyal SK, Krishna MGJC. Single and twinned plates of 2D layered BiI_3 for use as nanoscale pressure sensors. 2018;20(33):4857-4866.
40. Gao J, Xu Z, Chen S, Bharathi MS, Zhang YW. Computational understanding of the growth of 2D materials. *Adv Theory Simul*. 2018;1(11):1800085.
41. Liu M, Wang RY. Size-dependent melting behavior of colloidal In, Sn, and Bi nanocrystals. *Sci Rep*. 2015;5:16353.
42. Collins JB, Levine H. Diffuse interface model of diffusion-limited crystal growth. *Phys Rev B*. 1985;31(9):6119-6122.
43. Kolasinski KW. *Surface Science: Foundations of Catalysis and Nanoscience*. Hoboken, NY: John Wiley & Sons; 2012.
44. Waleed A, Tavakoli MM, Gu L, et al. All inorganic cesium lead iodide perovskite nanowires with stabilized cubic phase at room temperature and nanowire array-based photodetectors. *Nano Lett*. 2017;17(8):4951-4957.
45. Yorikawa H, Muramatsu S. Theoretical study of crystal and electronic structures of BiI_3. *J Phys Condens Matter*. 2008;20(32):325220.
46. Trotter J, Zobel T. The crystal structure of SbI3 and BiI3. *Z Kristallogr*. 1966;123(1–6):67-72.
47. Cuña A, Aguiar I, Gancharov A, et al. Correlation between growth orientation and growth temperature for bismuth tri-iodide films. *Cryst Res Technol*. 2004;39(10):899-905.
48. Brandt RE, Kurchin RC, Hoye RL, et al. Investigation of bismuth triiodide (BiI_3) for photovoltaic applications. *J Phys Chem Lett*. 2015;6(21):4297-4302.
49. Tiwari D, Alibhai D, Fermin DJ. Above 600 mV open-circuit voltage BiI_3 solar cells. *ACS Energy Lett*. 2018;3(8):1882-1886.
50. Repins I, Contreras MA, Egaas B, et al. 19.9%-efficient ZnO/-CdS/$CuInGaSe_2$ solar cell with 81.2% fill factor. *Prog Photovoltaics Res Appl*. 2008;16(3):235-239.
51. Braunger D, Hariskos D, Walter T, Schock H. An 11.4% efficient polycrystalline thin film solar cell based on $CuInS_2$ with a Cd-free buffer layer. *Sol Energy Mater Sol Cells*. 1996;40(2):97-102.

52. Islam MM, Ishizuka S, Yamada A, et al. CIGS solar cell with MBE-grown ZnS buffer layer. *Sol Energy Mater Sol Cells*. 2009; 93(6–7):970-972.
53. Noel NK, Stranks SD, Abate A, et al. Lead-free organic–inorganic tin halide perovskites for photovoltaic applications. *Energy Environ Sci*. 2014;7(9):3061-3068.
54. Xu M-F, Zhu X-Z, Shi X-B, et al. Plasmon resonance enhanced optical absorption in inverted polymer/fullerene solar cells with metal nanoparticle-doped solution-processable TiO_2 layer. *ACS Appl Mater Interfaces*. 2013;5(8):2935-2942.
55. Garnett E, Yang PJN. Light trapping in silicon nanowire solar cells. *Nano Lett*. 2010;10(3):1082-1087.

SUPPORTING INFORMATION

Additional supporting information may be found online in the Supporting Information section at the end of this article.

How to cite this article: Zhu Y, Zhang Q, Kam M, et al. Vapor phase fabrication of three-dimensional arrayed BiI_3 nanosheets for cost-effective solar cells. *InfoMat*. 2019;1–9. https://doi.org/10.1002/inf2.12070